PNAS

Cell size and polarization determine cytokinesis furrow ingression dynamics in mouse embryos

Lia Mara Gomes Paim[a] and Greg FitzHarris[a,b,c,1]

Cytokinesis is the final step of cell division during which a contractile ring forms a furrow that partitions the cytoplasm in two. How furrow ingression is spatiotemporally regulated and how it is adapted to complex cellular environments and developmental transitions remain poorly understood. Here, we examine furrow ingression dynamics in the context of the early mouse embryo and find that cell size is a powerful determinant of furrow ingression speed during reductive cell divisions. In addition, the emergence of cell polarity and the assembly of the apical domain in outer cells locally inhibits the recruitment of cytokinesis components and thereby negatively regulates furrow ingression specifically on one side of the furrow. We show that this biasing of cytokinesis is not dependent upon cell–cell adhesion or shape but rather is cell intrinsic and is caused by a paucity of cytokinetic machinery in the apical domain. The results thus reveal that in the mouse embryo cell polarity directly regulates the recruitment of cytokinetic machinery in a cell-autonomous manner and that subcellular organization can instigate differential force generation and constriction speed in different zones of the cytokinetic furrow.

cytokinesis | cell polarity | embryo development | contractile ring | furrow ingression

Cytokinesis is the final step of cell division, a multistep process initiated by signaling from the anaphase spindle midzone that induces the assembly and constriction of an actomyosin ring responsible for partitioning the cytoplasm in two (1, 2). Although many of the molecular players in furrow constriction have been identified, how furrow ingression is spatiotemporally regulated remains poorly understood. Moreover, little is known about how constriction is adapted to different cell contexts.

While many studies of cytokinesis use cultured cells, valuable insights can be gleaned from complex cellular systems. For instance, in epithelia cell–cell adhesion has been shown to mechanically regulate furrow ingression by anchoring the contractile ring to sites of cell adhesion, thereby restricting constriction on the apical side (3–6). Moreover, apical polarity has been proposed to contribute to furrow ingression positioning and dynamics during asymmetric cell divisions (7, 8), though how polarity controls cytokinesis, and how apical polarity and cell adhesion cooperate to regulate furrow ingression, are not well understood. One outstanding question to which complex systems have generated insight is how the contractile ring is organized and whether contractile forces are generated locally or globally throughout the ring. Interestingly, in the reductive cleavages of *Caenorhabditis elegans* embryos, it was found that cell-size reductions cause a progressive decline in contractile ring constriction speed (9–12). Based on this, a model was proposed wherein a greater number of locally regulated contractile units in bigger cells causes larger rings to constrict more rapidly than smaller ones (10). However, whether these observations extend to higher eukaryotes and what regulates furrow ingression dynamics in complex mammalian systems remain underexplored.

Here we address these questions in the niche context of early mouse embryo development, in which progressive cell-size reductions coincide with key morphogenetic events—such as the emergence of cell–cell adhesion patterns, apical polarity establishment, and cell-fate determination. In addition to a strong influence of cell size upon furrow ingression speed, we report that apical polarity limits the recruitment of cytokinesis components specifically on one side of the furrow, which serves as a cell-intrinsic mechanism for generating a laterally based cytokinesis.

Results

An Upper Limit to Cell-Size Scaling of Furrow Ingression in Mouse Embryos.
Although many of the molecules essential for the constriction of the actomyosin ring that in turn drives furrow ingression are known, what determines the speed of ring constriction is poorly understood. We set out to perform four-dimensional live cell imaging during

Significance

The final step of cell division, termed cytokinesis, comprises the constriction of a furrow that divides the cytoplasm to form two daughter cells. Although cytokinesis is well studied in traditional cell systems, how cytokinesis is regulated in complex multicellular settings and during cell-fate decisions is less well understood. Here, using live imaging and physical and molecular interventions, we find that the emergence of cell polarity during mouse embryo morphogenesis dramatically impacts cytokinesis mechanisms. Specifically, the assembly of the apical domain in outer cells locally inhibits the cytokinetic machinery, leading to an unexpected laterally biased cytokinesis.

the 1–2, 2–4, 4–8, 8–16, 16–32, and 32–64 cell divisions in mouse embryos, using GAP43:GFP plasma membrane labeling to measure the perimeter of the contractile ring during furrowing (Fig. 1 *A* and *B* and see also *SI Appendix*, Fig. S1). The speed at which the cytokinetic furrow constricted ("speed of constriction," expressed as a decrease in furrow perimeter in micrometers per minute) was constant for the majority of the duration of furrow ingression in any given cell, similar to other cells studied (10, 13, 14). We found that constriction speed is similar between the 1–2 and 8–16 cell divisions in mouse embryos (Fig. 1*C*) and, consequently, the duration of cytokinesis (see *Materials and Methods*) decreases between the 1–2 and 8–16 cell divisions (Fig. 1*D*). However, furrowing speed decreased between the 8–16 and 16–32 cell division ($P < 0.05$), with a further nonsignificant decrease in speed observed between the 16–32 and 32–64 cell stages (Fig. 1 *C* and *D*).

To explore whether the differences in furrow ingression speed we observed from the 8–16 cell stage onward might be due to changing cell size, we first set out to artificially reduce cytoplasmic volume using micromanipulation (*SI Appendix*, Fig. S2 *A–I* and see *Materials and Methods*). Although furrowing speed was similar between sham-manipulated controls and blastomeres with reduced cytoplasmic size (~40% reduction by volume) at the 4–8 cell division (sham: 12.22 ± 0.43 μm/min; reduced cytoplasm: 11.78 ± 0.52 μm/min; $P = 0.5222$) (Fig. 1 *E* and *F*), furrowing speed was substantially reduced in blastomeres undergoing the 8–16 cell division with reduced cytoplasmic size (sham: 11.22 ± 0.55 μm/min; reduced cytoplasm: 8.55 ± 0.30 μm/min; $P = 0.0004$) (Fig. 1 *G* and *H*). Notably, the distribution of constriction speeds measured in sham-manipulated controls and blastomeres with reduced cytoplasmic size at the 8–16 cell division followed an inverse correlation with initial perimeter at anaphase onset ($R^2 = 0.4930$; *SI Appendix*, Fig. S2*J*), indicating that cytoplasmic removal impacted furrowing proportional to the amount of cytoplasm removed.

Next, to investigate the impact of increased cell size, we employed an approach we previously developed to increase cell volume while maintaining the correct ploidy and cell division count (15), wherein cytokinesis was blocked at the 2–4 cell stage, and micromanipulation was then employed to remove the additional nucleus, thereby creating an embryo comprising two double-sized four-cell-stage blastomeres (*SI Appendix*, Fig. S3). Analysis of these embryos later in development showed that constriction speed was similar at the 8–16 cell division between sham-manipulated controls (10.63 ± 0.35 μm/min) and double-sized blastomeres (11.52 ± 0.41 μm/min; $P = 0.1118$) (Fig. 1 *I* and *J*), consistent with a lack of impact of cell size upon furrowing speed prior to the 16–32 cell stage. Notably however, at the 16–32 cell division, constriction speed was increased in double-sized blastomeres (7.76 ± 0.25 μm/min) as compared to controls (5.44 ± 0.23 μm/min; $P < 0.0001$; Fig. 1 *K* and *L*). Thus, increasing or decreasing cytoplasmic volume changes furrowing speed accordingly from the 8–16 cell stage onward. Whether this effect is a direct impact of cell size on the cytokinesis machinery, as previously alluded to in *C. elegans* embryos (10, 12) and *Neurospora crassa* (13), or whether cell size impacts constriction speed indirectly by influencing other cellular systems that affect the cytoskeleton remains to be determined. Nonetheless, this series of experiments suggest that cytokinesis furrowing speed is strongly influenced by cell size from the 8–16 cell stage onward.

Apical Polarity Emergence Decreases Outer Cell Constriction Speed Independently of Cell Fate. Early embryonic development is marked not only by lessening cell size but also by well-defined morphogenetic events (Fig. 2*A*). At the 8-cell stage, pulsatile forces generated by the actomyosin cortex coupled with E-cadherin–dependent restriction of contractility away from cell–cell contacts drive the onset of compaction (16, 17). The subsequent cell division gives rise to a 16-cell embryo composed of approximately spherical/cuboidal nonpolarized inner blastomeres, and flatter, polarized outer blastomeres that possess a characteristic apical domain (16, 18–20) (Fig. 2*A*). By the late 16-cell stage, the first cell fate decision is initiated, wherein the transcription factor TEAD4 is expressed in outer cells and induces the expression of the trophectoderm determinant CDX2 exclusively in those cells (16) (Fig. 2*A*). To address whether any of these events might cooperate with cell size to influence furrowing speed in embryos, we first compared furrowing speeds in inner cells and outer cells and found that, both at the 16–32 and 32–64 cell divisions, outer cells had a significantly reduced furrowing speed compared to inner cells (16–32 outer: 5.39 ± 0.15 μm/min; 32–64 outer: 4.71 ± 0.67 μm/min; 16–32 inner: 7.71 ± 0.42 μm/min; 32–64 inner: 6.39 ± 0.24 μm/min; 16–32 $P = 0.0004$; 32–64 $P = 0.0081$) (Fig. 2 *B* and *C*). We wondered whether the slowed furrowing of outer cells might be a result of the different shapes of inner and outer cells, outer cells being predominantly more flattened than inner cells. To test this, we abolished cell adhesion in embryos undergoing the 16–32 cell division using Ca^{+2}-free media (*SI Appendix*, Fig. S4*A*). Importantly, removal of Ca^{+2} from the culture media did not prevent apical polarity establishment, as evidenced by the enrichment of the polarity marker PKCζ in the apical surface of outer cells (*SI Appendix*, Fig. S4 *B* and *C*) and embryos were able to undergo the 16–32C transition (*SI Appendix*, Fig. S4 *D* and *E* and Movie S1), but in the absence of cell–cell adherence all cells adopted a rounded shape. Notably, outer cells still displayed reduced speed of constriction (6.02 ± 0.39 μm/min) as compared to inner cells (7.42 ± 0.27 μm/min; $P = 0.0062$) (Fig. 2 *D* and *E*). Thus, the slower furrowing speed of outer cells relative to inner cells is not due to their flattened shape or cell–cell adhesion but is rather due to an intrinsic property of the cells.

We next wondered whether the emergence of cell polarity and the formation of the apical domain might be responsible for the decrease in speed of constriction of outer cells. To address this, we depleted the apical polarity protein PARD6B using short hairpin RNAs (shRNA). PARD6B shRNA efficiently disrupted apical polarity emergence, as evidenced by the absence of the apical domain marker PKCζ (Fig. 2 *F* and *G*), as previously described (21, 22). Strikingly, following PARD6B depletion, furrowing speed in outer cells increased to a velocity comparable to that of inner cells (7.04 ± 0.23 μm/min vs. 6.65 ± 0.20 μm/min, $P = 0.7127$) (Fig. 2 *H* and *I*), suggesting that the emergence of apical polarity in outer cells negatively impacts furrow dynamics. Formation of the apical domain contributes to cell-fate determination in the early embryo by allowing the transcriptional activation of TEAD4 in outer cells at the 16-cell stage (16, 23). Therefore, to determine whether the impact of the apical domain on furrowing speed might relate to cell fate, we depleted TEAD4 by double-stranded RNA (dsRNA) injections (23) and analyzed the speed of constriction of inner and outer cells at the 16–32 cell division. TEAD4 dsRNA knockdown efficiency was confirmed by the absence of TEAD4 nuclear localization with immunofluorescence (*SI Appendix*, Fig. S5 *A* and *B*), as previously described (23), and its depletion did not prevent apical polarity emergence at the 16-cell stage as evidenced by the enrichment of the polarity marker PKCζ in the apical surface of outer cells (*SI Appendix*, Fig. S5*C*). Notably, outer cells
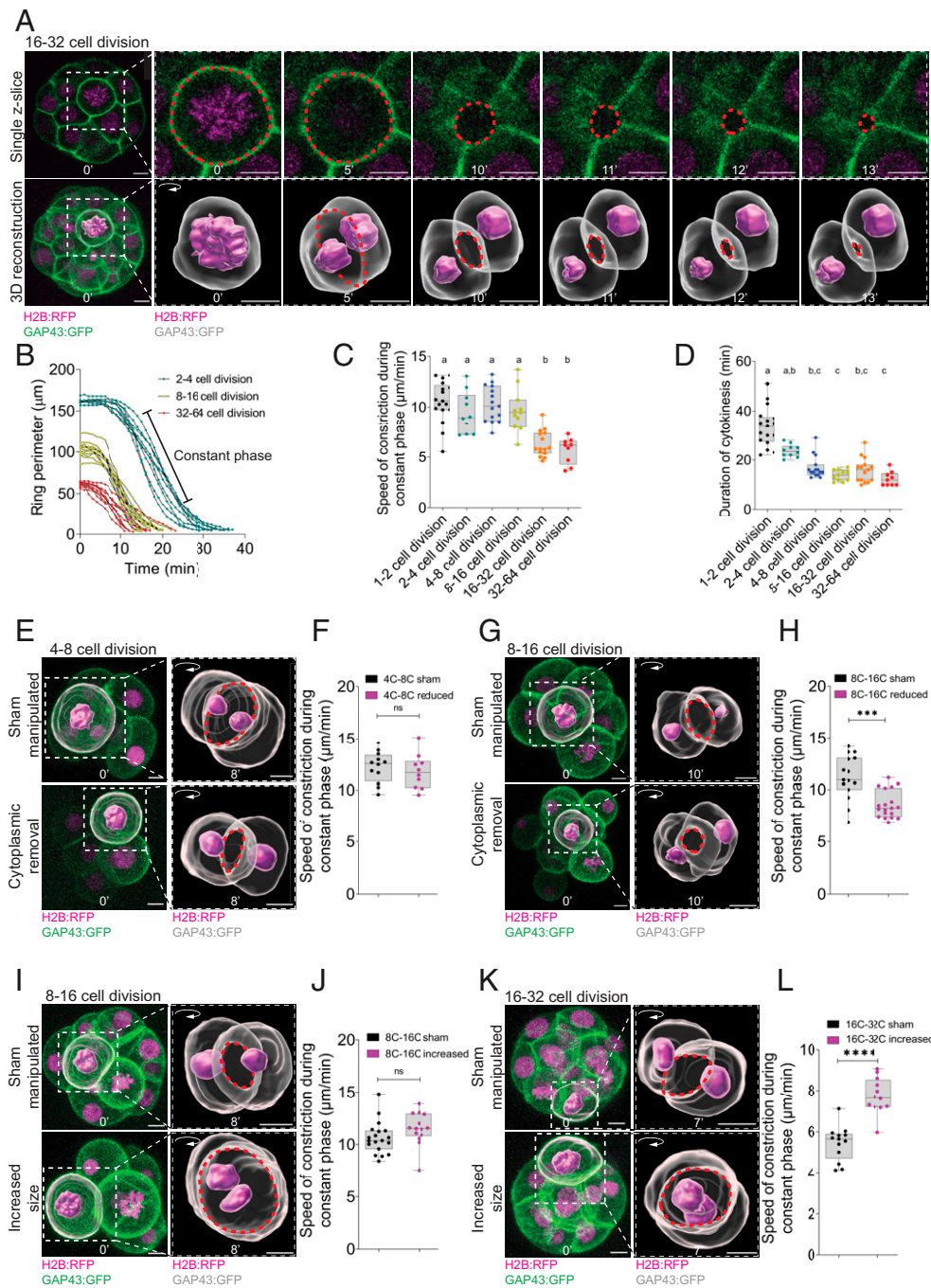
Fig. 1. Cell size determines furrowing speed from the eight-cell stage in mouse embryos. (*A*) Single z-slice (*Top*) and three-dimensional reconstructions (*Bottom*) of a cell undergoing the 16–32 cell division (example shown has 26 cells) coexpressing H2B:RFP (magenta) and GAP43:GFP (green/gray). Red dashed circles indicate where the measurements of contractile ring perimeter were performed. (*B*) Quantification of contractile ring perimeter in blastomeres undergoing the 2–4 (*n* = 10 blastomeres from 10 embryos), 8–16 (*n* = 11 blastomeres from 8 embryos), and 32–64 cell divisions (*n* = 9 blastomeres from eight embryos). Individual curves represent independent blastomeres. (*C* and *D*) Quantification of average speed of ring constriction during the constant phase of perimeter decrease (one-way ANOVA with multiple comparisons) (*C*) and duration of cytokinesis (Kruskal–Wallis with multiple comparisons) (*D*) at the 1–2 (*n* = 17 blastomeres from 17 embryos), 2–4 (*n* = 10 blastomeres from 10 embryos), 4–8 (*n* = 15 blastomeres from 12 embryos), 8–16 (*n* = 11 blastomeres from 8 embryos), 16–32 (*n* = 15 blastomeres from 11 embryos), and 32–64 cell divisions (*n* = 9 blastomeres from eight embryos). (*E* and *G* and see also *SI Appendix*, Fig. S2 *A–I*) Representative time-lapse three-dimensional reconstruction of a cell in a sham-manipulated and embryo with reduced cytoplasmic size undergoing the 4–8 (example in sham has seven cells and reduced size has six cells) (*E*) and 8–16 cell divisions (example in sham has 8 cells and reduced size has 13 cells) (*G*) coexpressing H2B:RFP (magenta) and GAP43:GFP (green/gray). (*F* and *H*) Quantification of average speed of constriction at the 4–8 (sham-manipulated *n* = 12 blastomeres from 11 embryos; cytoplasmic removal *n* = 10 blastomeres from 9 embryos; two-tailed unpaired *t* test, *P* = 0.5222) (*F*) and 8–16 cell divisions (sham-manipulated *n* = 15 blastomeres from 8 embryos; cytoplasmic removal *n* = 19 blastomeres from 10 embryos; two-tailed Mann–Whitney *U* test, ****P* = 0.0004) (*H*). (*I* and *K*) Representative time-lapse three-dimensional reconstructions of cells undergoing the 8–16 cell division from sham-manipulated (*Top*; example shown has 12 cells) or embryos with increased cytoplasmic size (*Bottom*; example has six cells) (*I*) and cells undergoing the 16–32 cell division from sham-manipulated (*Top*; example has 18 cells) or embryos with increased cytoplasmic size (*Bottom*; example has 13 cells) (*K*). (*J* and *L*) Quantification of average speed of constriction of blastomeres from sham-manipulated or embryos with increased cytoplasmic size at the 8–16 (sham *n* = 19 blastomeres from 11 embryos; increased *n* = 14 blastomeres from 9 embryos; two-tailed unpaired *t* test nonsignificant (ns) *P* = 0.1118 (*J*) and outer blastomeres at 16–32 cell divisions (sham *n* = 13 blastomeres from 7 embryos; increased *n* = 12 blastomeres from 9 embryos; two-tailed unpaired *t* test *****P* < 0.0001. Time is shown in minutes, where 0′ is anaphase onset. (Scale bars, 10 μm.) In the box plots, the center line represents the median, the bounds of the box represent upper and lower quartiles, the whiskers represent minimum and maximum values, and dots represent independent measurements. In multiple comparison analyses, different letters represent statistical significance at *P* < 0.05.
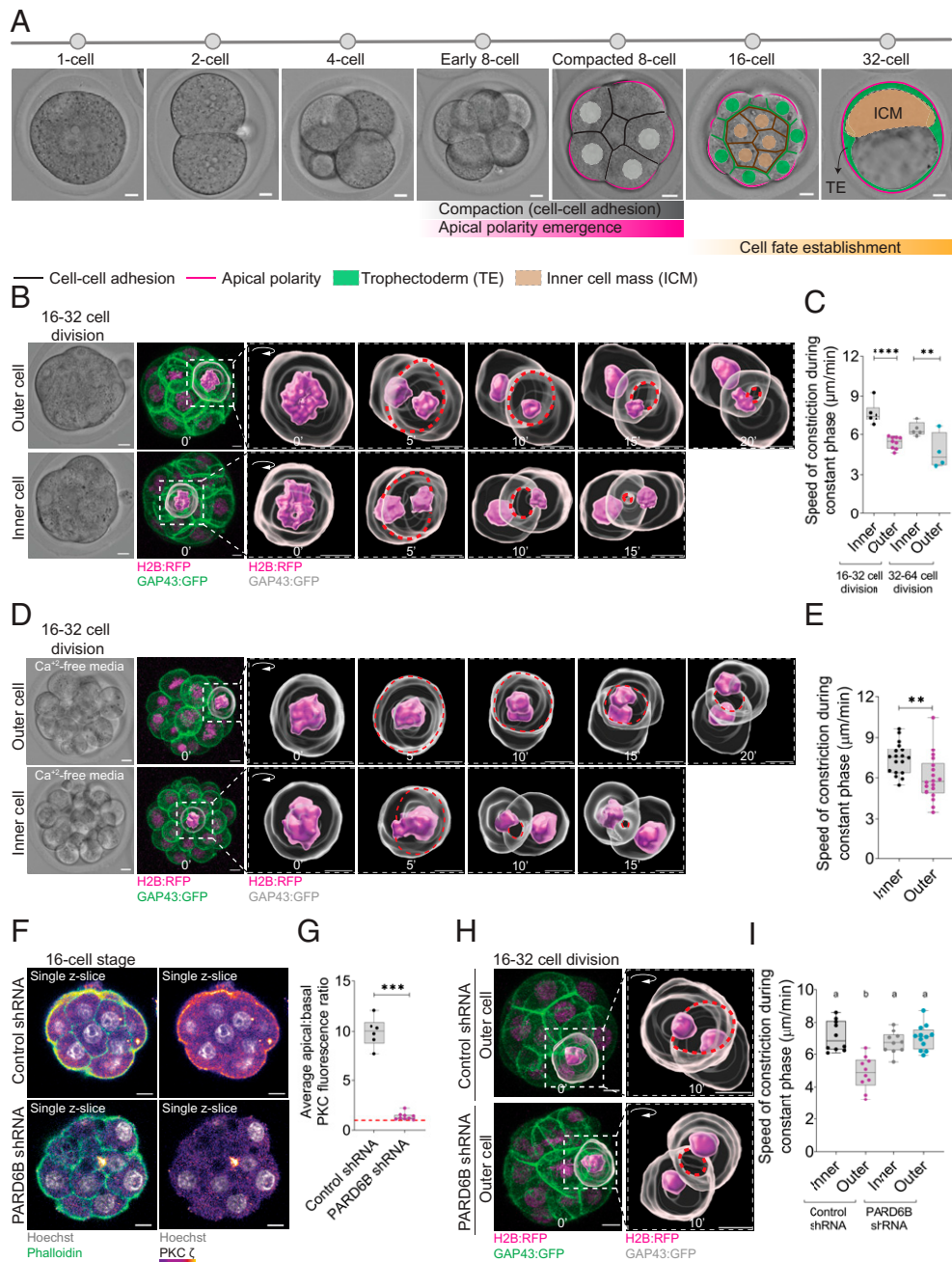
Fig. 2. Apical polarity reduces the speed of constriction of outer cells independently of cell shape and adhesion. (*A*) Illustration of morphogenetic events of mouse preimplantation development. E-cadherin accumulation at the basolateral surface drives compaction at the eight-cell stage, concomitantly with the emergence of apical polarity. The resulting 16-cell embryo displays outer cells that are polarized and flat and inner cells that are cuboidal and apolar and undergoes lineage specification, wherein most outer cells are destined to trophectoderm specification whereas inner cells are directed to the inner cell mass (ICM). (*B*) Representative bright-field and time-lapse three-dimensional (3D) reconstructions of outer and inner cells undergoing the 16–32 cell division (example shown for outer cell has 16 cells and for inner cell has 24 cells) coexpressing H2B:RFP (magenta) and GAP43:GFP (green/gray). (*C*) Quantification of average speed of constriction of inner and outer cells at 16–32 (inner $n = 6$ blastomeres; outer $n = 9$ blastomeres from 11 embryos) and 32–64 cell divisions (inner $n = 5$ blastomeres; outer $n = 4$ blastomeres from eight embryos; one-way ANOVA comparing means of preselected columns, ****$P < 0.0001$, **$P = 0.0081$). The data quantified in *C* were obtained from the same embryos in Fig. 1 *B–D*. (*D*) Representative bright-field and time-lapse 3D reconstructions of outer and inner cells undergoing the 16–32 cell division (example for outer cell has 21 cells and for inner cell has 30 cells) coexpressing H2B:RFP (magenta) and GAP43:GFP (green/gray) cultured in Ca^{+2}-free media. (*E*) Quantification of average speed of constriction of inner ($n = 18$ blastomeres) and outer blastomeres ($n = 18$ blastomeres from total of 18 embryos; two-tailed unpaired *t* test, **$P = 0.0062$) undergoing the 16–32 cell division from embryos cultured in Ca^{+2}-free media. (*F*) Representative immunofluorescence images of 16-cell embryos previously injected with either control shRNA (*Top*) or PARD6B shRNA (*Bottom*). (*G*) Quantification of average apical:basal PKCζ fluorescence ratio in 16-cell embryos previously injected with either control shRNA ($n = 6$ embryos) or PARD6B shRNA ($n = 9$ embryos; two-tailed Mann–Whitney *U* test, ***$P = 0.0004$). (*H*) Representative time-lapse 3D reconstructions of outer blastomeres undergoing the 16–32 cell division from embryos previously injected with control shRNA (*Top*; example has 17 cells) or PARD6B shRNA (*Bottom*; example has 20 cells) and coexpressing H2B:RFP (magenta) and GAP43:GFP (green/gray). (*I*) Quantification of average speed of constriction of inner and outer blastomeres undergoing the 16–32 cell division from embryos previously injected with control shRNA (inner $n = 10$ blastomeres; outer $n = 10$ blastomeres from a total of 12 embryos) or PARD6B shRNA (inner $n = 10$ blastomeres; outer $n = 12$ blastomeres from a total of 10 embryos; one-way ANOVA with multiple comparisons). Time is shown in minutes, where 0′ is anaphase onset. (Scale bars, 10 μm.) In the box plots, the center line represents the median, the bounds of the box represent upper and lower quartiles, the whiskers represent minimum and maximum values, and dots represent independent measurements.

from TEAD4-depleted embryos still displayed reduced speed of constriction (6.98 ± 0.23 μm/min) as compared to inner cells (9.75 ± 0.28 μm/min; $P = 0.0022$), similar to controls (inner: 9.06 ± 0.35 μm/min; outer: 6.47 ± 0.23 μm/min; $P = 0.0010$) (*SI Appendix*, Fig. S5 *D and E*). Thus, the emergence of the apical domain lessens furrowing speed in outer cells independently of the downstream impact on cell fate.

Apical Polarity Laterally Biases Furrow Ingression Independently of Cell Adhesion. In 16–32 cell-stage embryos, outer cell divisions are oriented either circumferentially or radially relative to the surface of the embryo (Fig. 3*A*). Circumferential cell divisions generate two new outer-residing cells immediately after cytokinesis completion, whereas radial cell divisions generate one inner-residing and one outer-residing cell (16, 24–26). Importantly, whereas radial divisions typically cause the apical domain to be asymmetrically inherited by the outer cell, circumferential divisions occur such that the contractile ring cuts through the apical domain and causes it to be symmetrically inherited by both daughter cells (Fig. 3*A*) (18). To better gauge the impact of polarity on cytokinesis in outer cells we therefore examined furrow ingression in relation to division orientation. Analysis of circumferential cell divisions demonstrated that the basal side of the furrow ingressed more quickly than the apical side (Fig. 3 *B–D, Top*), resulting in a total displacement of 17.37 ± 2.30 μm from the basal side and 8.71 ± 0.57 μm from the apical side (Fig. 3 *B–D*, first row; $P = 0.0327$). Strikingly, this basal-to-apical ingression bias was abolished in circumferential outer cell divisions upon PARD6B knockdown (total displacement apical side: 10.88 ± 0.73 μm; total displacement basal side: 13.28 ± 0.90 μm; $P = 0.1514$) (Fig. 3 *B–D*, third row and *SI Appendix*, Fig. S6). In contrast, in radial cell divisions both sides of the furrow ingressed similarly both in controls (total displacement side 1: 12.96 μm ± 1.44; total displacement side 2: 12.43 μm ± 1.77; $P = 0.8209$) as well as in PARD6B-depleted embryos (total displacement side 1: 12.37 μm ± 0.90; total displacement side 2: 13.73 μm ± 1.04; $P = 0.9290$) (Fig. 3 *B–D*, second and fourth rows and *SI Appendix*, Fig. S6).

A basal-to-apical cytokinesis ingression bias has previously been observed in both *Drosophila melanogaster* and mammalian epithelial cells (3–6, 27). Notably, however, in the case of *D. melanogaster* epithelial cells, cell–cell adhesion drives the bias via mechanical anchorage of the contractile ring to E-cadherin complexes, thus hampering furrow ingression on the apical side (3–6). Thus, to further probe whether the bias observed in outer blastomeres was indeed caused by an inhibitory effect of the apical domain on the cytokinesis machinery rather than cell–cell adhesion, we analyzed furrow ingression dynamics in circumferentially and radially dividing outer blastomeres at the 16–32 cell transition from embryos relieved of cell–cell adhesion via exposure to Ca^{+2}-free media (Fig. 3 *E–G*). Similarly to our previous results, a basal-to-apical bias of furrow ingression was detected exclusively in circumferentially dividing outer blastomeres of embryos devoid of cell–cell adhesion (total displacement apical side: 10.97 μm ± 0.94; total displacement basal side: 15.91 μm ± 0.98; $P = 0.0264$) and not in radially dividing blastomeres (total displacement side 1: 15.18 μm ± 0.92; total displacement side 2: 13.36 μm ± 0.65; $P = 0.2026$) (Fig. 3 *E–G*). We conclude that the overall slowing of ring constriction speed in outer cells is a result of reduced ingression specifically on the apical side during circumferential cell divisions, by a mechanism that is cell-intrinsic and not dependent on cell adhesion or shape.

Apical Polarity Disrupts the Recruitment of Furrowing Regulators in a Cell-Autonomous Manner. To understand why the apical domain might slow furrow ingression, we sought to visualize the distribution of cytokinesis components at the contractile ring during cytokinesis in circumferentially dividing outer cells. To do this, we applied a correlative live-fix imaging approach (28, 29), in which we first performed live imaging of control and PARD6B-depleted embryos at the 16–32 cell division expressing H2B:RFP to visualize cytokinesis and then fixed them specifically at midcytokinesis to further perform immunofluorescence of established cytokinesis regulators. Consistent with previous reports (18, 30), a focused apical domain was retained during M-phase in control embryos, as evidenced by the enrichment of polarity protein PKCζ in the apical surface at midcytokinesis (Fig. 4 *A* and *C*). Strikingly, in control embryos, Anillin and p-Myosin were asymmetrically distributed within the contractile ring, being enriched in regions where it overlapped with the basolateral domain, but substantially decreased where it overlapped with the PKCζ-positive apical domain (apical:basal ratio Anillin: 0.28 ± 0.05; p-Myosin: 0.31 ± 0.05; Fig. 4 *A–D* and *SI Appendix*, Fig. S7 *A and B*). This asymmetric distribution within the contractile ring was lost upon PARD6B knockdown, wherein the PKCζ-labeled apical domain was no longer evident, and Anillin and p-Myosin became evenly distributed (apical:basal ratio Anillin: 0.86 ± 0.04; p-Myosin: 0.96 ± 0.08; Fig. 4 *A–D*; *SI Appendix*, Fig. S7 *A and B*). The sum of fluorescence intensity of both apical and basal sides was similar between control (Anillin: 87.78 ± 16.41 arbitrary units [a.u.]; p-Myosin: 126.6 ± 12.86 a.u.) and PARD6B-depleted embryos (Anillin: 103.9 ± 22.48 a.u. $P = 0.6881$; p-Myosin: 118.7 ± 15.08 a.u. $P = 0.7006$; *SI Appendix*, Fig. S7 *C and D*), suggesting that the impact of polarity emergence was to bias the localization of Anillin and p-Myosin rather than affect their overall levels. To address whether asymmetric distribution of cytokinesis regulators could be mediated by cell adhesion rather than apical polarity, we performed correlative live-fix imaging of embryos at the 16–32 cell division treated with Ca^{+2}-free media to abolish cell adhesion and assessed the levels of Anillin at the contractile ring by immunofluorescence. Notably, Anillin was substantially underrepresented where the contractile ring overlapped with the apical domain and enriched at the basal side (Anillin apical:basal ratio: 0.35 ± 0.04; significant deviation from 1, $P < 0.0001$; Fig. 4 *E* and *F* and *SI Appendix*, Fig. S7 *E*). These results corroborate the notion that the inhibitory effect of apical polarity on the cytokinetic machinery is a cell-autonomous effect that is not dependent on cell–cell contacts (Fig. 4 *G*). The asymmetric localization of cytokinesis components was observed exclusively in dividing blastomeres undergoing cytokinesis, whereas interphase localization of Anillin (nuclear) and p-Myosin (undetectable/cytoplasmic) remained unaffected (Fig. 4 *A*, *C*, and *E*, third panels), suggesting that the apical domain most likely impacts the localization of cytokinesis components solely during cytokinesis. Thus, the emergence of the apical domain in outer cells prevents accumulation of cytokinesis components including Anillin and p-Myosin during cytokinesis, leading to an unbalanced furrow ingression which is slowed specifically on the apical side.

Discussion

Exploiting multiple well-characterized developmental transitions in the early mouse embryo, our work delineates two powerful influences on furrow ingression speed, both of which have
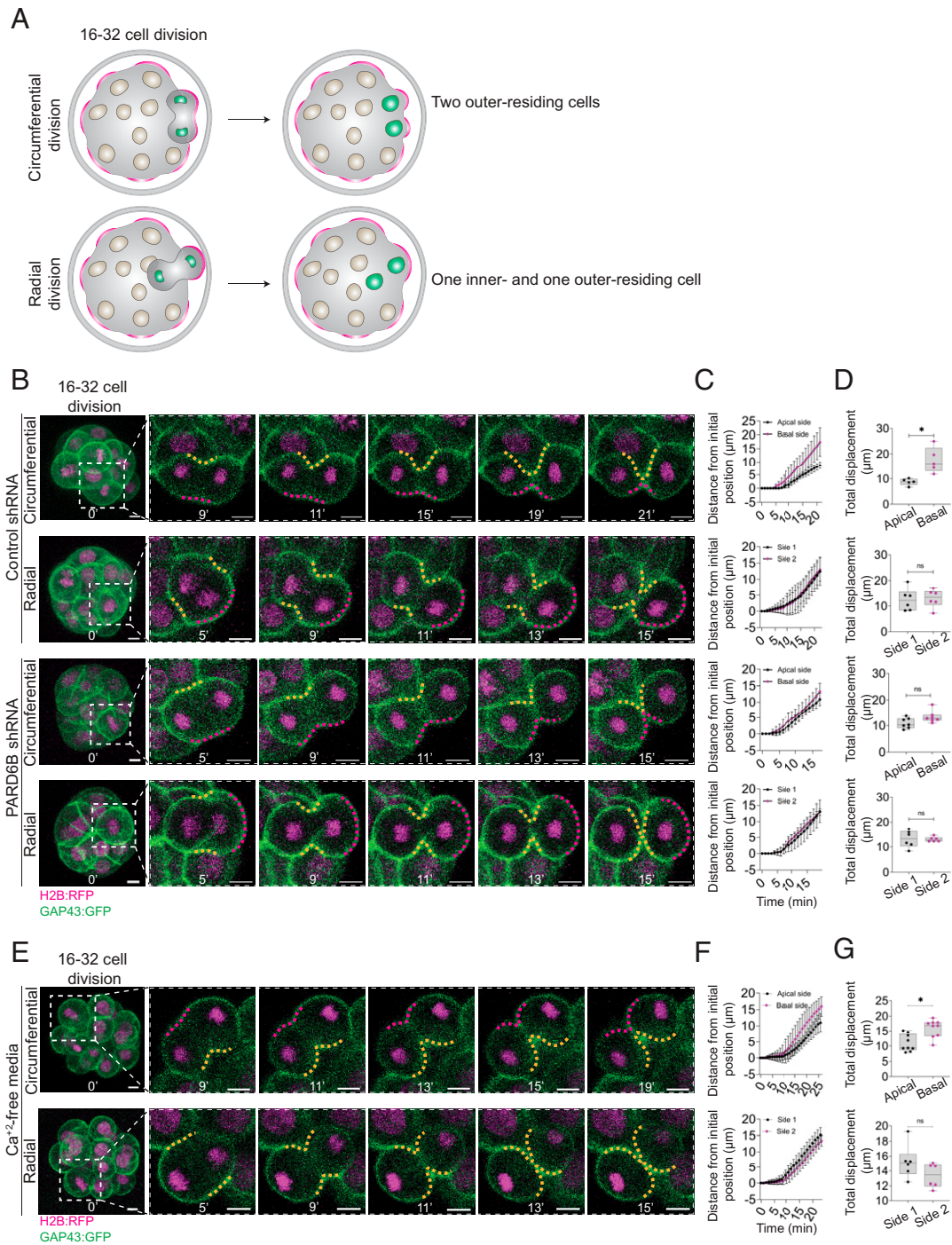
Fig. 3. Apical polarity biases furrow ingression independently of cell adhesion. (*A*) Illustration of cell division orientation in outer cells at the 16–32 cell transition. Outer cells divide either circumferentially, generating two new outer-residing cells, or radially, generating one inner-residing and one outer-residing cell. Note that circumferential cell divisions occur such that the contractile ring cuts through the apical domain and can lead to symmetric inheritance of the apical domain. (*B*) Representative time-lapse images of circumferentially and radially dividing blastomeres undergoing the 16–32 cell division from embryos previously injected with either control shRNA (examples shown for both circumferential and radial divisions have 23 cells) or PARD6B shRNA (example shown for circumferential division has 21 cells and for radial has 16 cells) and coexpressing H2B:RFP (magenta) and GAP43:GFP (green). Magenta dashed lines indicate the location of the apical domain, and yellow dashed lines indicate the regions that do not contain an apical domain. (*C*) Average distance from initial furrow position at anaphase onset in circumferentially or radially dividing blastomeres undergoing the 16–32 cell division from embryos previously injected with control (circumferential: n = 5 blastomeres from five embryos; radial: n = 6 blastomeres from five embryos) or PARD6B shRNA (circumferential: n = 7 blastomeres from five embryos; radial: n = 6 blastomeres from five embryos). (*D*) Total furrow displacement of blastomeres from embryos in *C*, dividing circumferentially (control: *P = 0.0327; PARD6B: ns [not significant] P = 0.1514) or radially (control: ns P = 0.8209; PARD6B: ns P = 0.9290; two-tailed paired t tests). (*E*) Representative time-lapse images of circumferentially and radially dividing blastomeres undergoing the 16–32 cell division from embryos coexpressing H2B:RFP (magenta) and GAP43:GFP (green) and cultured in Ca^{+2}-free media (example shown for circumferential division has 21 cells and for radial division has 19 cells). Magenta dashed lines indicate the location of the apical domain, and yellow dashed lines indicate the regions that do not contain an apical domain. (*F*) Average distance from initial furrow position at anaphase onset in circumferentially (n = 9 blastomeres from eight embryos) or radially dividing blastomeres (n = 6 blastomeres from six embryos) undergoing the 16–32 cell division from embryos cultured in Ca^{+2}-free media. (*G*) Total furrow displacement of blastomeres from embryos in *F*, dividing circumferentially (two-tailed paired t test, *P = 0.0264) or radially (two-tailed paired t test, ns P = 0.2026). Time is shown in minutes, where 0′ is anaphase onset. (Scale bars, 10 μm.) In the box plots, the center line represents the median, the bounds of the box represent upper and lower quartiles, the whiskers represent minimum and maximum values, and dots represent independent measurements.
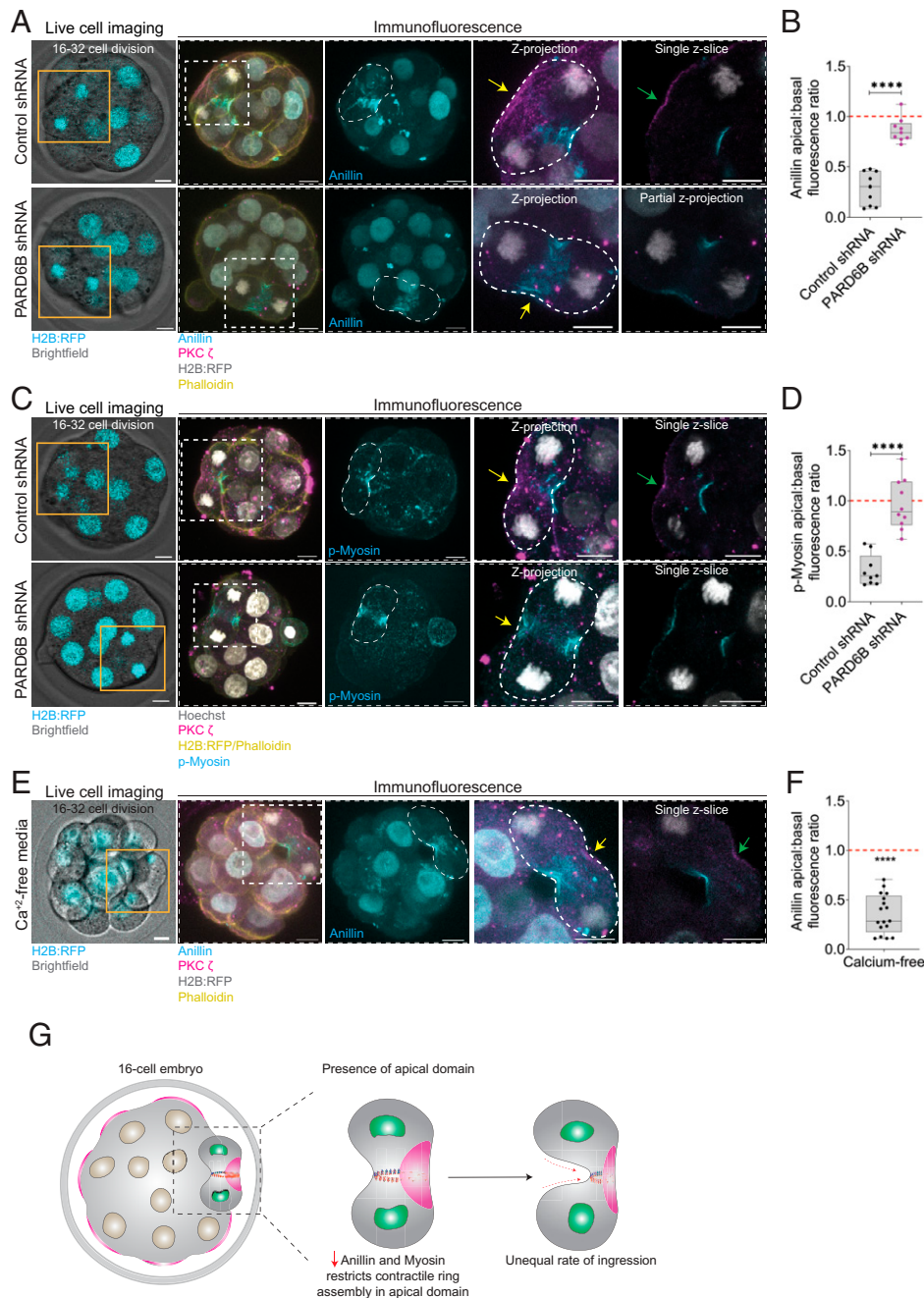
Fig. 4. Apical polarity disrupts the recruitment of furrowing regulators independently of cell adhesion. (*A* and *C*) Representative live and immunofluorescence images of circumferentially dividing blastomeres undergoing the 16–32 cell division from embryos previously injected with control (example shown in *A* has 19 cells and in *C* has 16 cells) or PARD6B shRNA (example shown in *A* has 16 cells and in *C* has 16 cells). Note that both Anillin (*A*) and p-Myosin (*C*) are underrepresented at the side of contractile ring that overlaps with the apical domain in controls, and this bias is abolished upon PARD6B depletion (yellow arrows). Also note that the apical domain is intact during division in controls (green arrows). (*B*) Apical:basal fluorescence ratio of Anillin in outer blastomeres undergoing the 16–32 cell division from embryos previously injected with control (*n* = 9 blastomeres from nine embryos) or PARD6B shRNA (*n* = 9 blastomeres from nine embryos; unpaired two-tailed *t* test, ****P < 0.0001). (*D*) Apical:basal fluorescence ratio of p-Myosin in outer blastomeres undergoing the 16–32 cell division from embryos previously injected with control (*n* = 9 blastomeres from nine embryos) or PARD6B shRNA (*n* = 10 blastomeres from 10 embryos; unpaired two-tailed *t* test, ****P < 0.0001). (*E*) Representative live and immunofluorescence images of a circumferentially dividing blastomere undergoing the 16–32 cell division from a H2B:RFP-expressing embryo cultured in Ca^{+2}-free media, in which the furrow overlaps with the apical domain (example has 16 cells). Note that Anillin was underrepresented at the apical side (yellow arrow) and the apical domain is intact during division (green arrow). (*F*) Apical:basal fluorescence ratio of Anillin in outer blastomeres undergoing the 16–32 cell division from embryos cultured in Ca^{+2}-free media (*n* = 17 blastomeres from 17 embryos, one-sample *t* test, ****P < 0.0001 significant deviation from 1). (*G*) Model for local regulation of ring constriction by the apical domain. In intact 16-cell embryos, apical polarity restricts the access of Anillin and p-Myosin to the contractile ring in circumferentially dividing outer cells, thereby slowing furrow ingression specifically on the side of the contractile ring that overlaps with the apical domain. Time is shown in minutes, where 0′ is anaphase onset. (Scale bars, 10 μm.) In the box plots, the center line represents the median, the bounds of the box represent upper and lower quartiles, the whiskers represent minimum and maximum values, and dots represent independent measurements.

broad ramifications for our understanding of the mechanism of ring ingression in diverse cell types. First, our data show a strong influence of cell size on furrow ingression from the 8–16 cell division onward. A similar cell-size to cytokinesis speed correlation in *C. elegans* (9–12) and *N. crasa* (13) was previously proposed as evidence that the contractile ring is locally

regulated, bigger rings contracting more quickly because they comprise larger numbers of locally regulated units that disassemble during furrowing. Our results extend the relationship between cell size and furrowing speed to the mouse preimplantation embryo. The insensitivity of furrowing speed to cell size from the 1–2 to 8–16 cell divisions suggests an upper limit of cell size beyond which furrowing speed cannot be further scaled up, and it is possible that this upper limit is not reached in one-cell *C. elegans* embryos which are more similar in volume to eight-cell-stage mouse blastomeres. An upper limit has been previously shown to restrict the scaling of spindle length in *Xenopus laevis* (31) and *C. elegans* embryos (32, 33). Given that the speed of chromosome separation and spindle elongation during anaphase is reduced from the eight-cell stage onward (34), altered furrowing speed may help avoid chromosome segregation error at later developmental stages.

Second, restricted furrowing in the apical domain was found to be the result of limited access of contractile ring components. This effect of the apical domain is independent of its role on cell fate determination, as determined by a lack of effect of TEAD4-knockdown (*SI Appendix*, Fig. S5), and consistent with this we also found a failure in the recruitment of Anillin and p-Myosin to the apical side of the contractile ring in circumferentially dividing blastomeres at the 8–16 cell division, in which apical polarity has already been established but cell fate is not yet determined (*SI Appendix*, Fig. S8). Limited myosin levels at the apical surface have also been observed in nondividing outer blastomeres and are thought to influence cell position and cell fate specification by reducing contractility to limit outer cell internalization and thus ensure adequate proportions of inner and outer blastomeres (35). Although the abundance of cytokinetic components has been previously correlated with ingression speed in asymmetrically ingressing furrows (5, 36, 37), our unexpected discovery that a similar bias in mouse embryos is due to the emergence of the apical domain allowed us to experimentally relieve that bias, and therein show directly that the abundance of Anillin and p-Myosin determines furrow ingression speed. Whether the inhibitory effect of polarity also affects other tissues in the mouse remains to be addressed. Nonetheless this series of experiments provide some of the strongest evidence that cell-autonomous subcellular organization can dictate local regulation of furrow ingression (Fig. 4G).

Our data also demonstrate that the inhibitory impact of the apical domain upon furrow ingression is not dependent on cell contacts, as embryos devoid of cell adhesion also display a basal-to-apical ingression bias and reduced Anillin localization to the apical side. This is distinct from previously noted links between furrowing and cell polarity described in *D. melanogaster* polarized epithelial cells, wherein cell adhesion promotes an anchoring of the contractile ring to E-cadherin complexes and reduce furrow ingression at the apical side independently of apical polarity (6). The phenomenon described herein is also distinct from that observed in *C. elegans* zygotes wherein apical PAR proteins promote the retention of Anillin and Septin at the anterior pole during an asymmetric division, possibly as a means to prevent an overload of cytokinesis regulators in the ingressing furrow in the first cell division (7). Why cytokinesis regulators are chased from the apical cortex during cytokinesis in mouse blastomeres remains to be seen, but an intriguing precedent is found in the observation that ECT2, the GEF responsible for activating cytokinesis master-regulator RhoA, and RhoA downstream effectors Rock1/2 can interact with polarity proteins (38, 39), albeit that whether these interactions might result in an inhibitory effect on cytokinesis components remains to be addressed. Alternatively, unidentified apical domain components may outcompete cytokinesis components for limited membrane binding sites. Our experiments highlight the complexity of furrow ingression regulation and underscore that cellular contexts and asymmetries can have stark impacts upon the mechanisms of cytokinesis.

Materials and Methods

Experimental Model. All experiments performed followed the guidelines for animal experimentation and were approved by the Comité Institutionnel de Protection des Animaux of the Centre de Recherche du Centre Hospitalier de l'Université de Montréal (protocol number: IP18034GFs). The female mice used in this study were 2- to 3-mo-old CD1 [Crl:CD1(ICR) 022CD1] and male mice were 3- to 12-mo-old BDF1 (B6D2F1/J 100006). All animals were kept in individually ventilated cages (up to five animals per cage for the females and one animal per cage for the males) at $22 \pm 2\,°C$, 40 to 60% humidity in 12-h light/dark cycles with lights switched on from 6:30 AM to 6:30 PM and food and water available for ad libitum consumption.

Embryo Collection and Culture. Two-cell embryos were harvested from previously superovulated 2- to 3-mo-old female CD1 mice mated with BDF1 male mice, except for the experiment in Fig. 1 *A–D* (one-cell stage group), in which embryos were harvested at the zygote stage. Embryos were collected in homemade M2 media and cultured in KSOM (MR-020P-5F; EMD Millipore) in 5% CO_2 at 37 °C. For experiments in Figs. 2 *D* and *E*, 3 *E–G*, 4 *E* and *F*, and *SI Appendix*, Fig. S4, 16-cell embryos were exposed to either complete homemade KSOM or Ca^{+2}-free homemade KSOM (*SI Appendix*, Table S1) during the 16–32 cell division.

Messenger RNA, shRNA, and dsRNA production. Messenger RNA (mRNA) was synthesized using Ambion mMessage Machine T3 (AM1348) or SP6 (AM1340) according to the manufacturer's instructions from the following plasmids: H2B:RFP in pRN4 (gift from Alex McDougal, Observatoire Océanologique de Villefranche sur Mer, Villefranche sur Mer, France) and GAP43:GFP in psC2 (gift from Yojiro Yamanaka, McGill University, Montréal, Canada). Knockdown of PARD6B via shRNA and TEAD4 via dsRNA was performed following previously described protocols (21–23). shRNA plasmids were purchased from Millipore Sigma (Control shRNA SHC002; PARD6B shRNA SHCLND-NM_021409 TRCN0000054687) and purified using QIAGEN Miniprep kit (27106). For dsRNA production, a Tead4 specific PCR primer pair including T7-derived RNApol promoters was used to obtain the in vitro transcription template using mouse blastocyst cDNA (sense; TAATACGACTCACTATAGGGTGTTGGAGTTCTCGGCTTTC, antisense; TAATACGACTCACTATAGGGTCGGTAGATGTGGTGCTGAG, T7-promoter underlined) (23). For the control group, a GFP specific dsRNA was produced with PCR primers including a T7 promoter (sense; TAATACGACTCACTATAGGGGAGAGTACAAATTTCTGTCAGTGGAGAGG, antisense; TAATACGACTCACTATAGGGGAGATGTATAGTTCATCCATGCCATGTGTA, T7-promoter underlined) (23) using pcDNA3.1 plasmid vector containing a GFP sequence as a template. Tead4 and GFP specific double-stranded RNA synthesis was performed using Ambion mMessage Machine T7 (AM1344) according to the manufacturer's instructions.

Microinjection, Cytoplasmic Removal, and Enucleation. Cytoplasmic microinjection of mRNAs or dsRNAs in two-cell embryos or zygotes was performed in M2 media (M7167; Sigma) using a picopump (World Precision Instruments) and micromanipulators (Narishige) mounted on a Leica DMI4000 inverted microscope (40). For shRNA microinjections in Figs. 2 *F–I*, 3 *B–D*, 4 *A–D*, and *SI Appendix*, Figs. S6 and S7, shRNA plasmids were microinjected directly inside both nuclei of two-cell embryos. Prior to microinjection, shRNA plasmids were diluted to 20 ng/μL in homemade microinjection buffer (5 mM Tris pH 7.4 and 0.1 mM ethylenediaminetetraacetic acid) and Fluorescin Dextran 70 kDa (FD70S; Sigma) 0.01 mg/mL was added to the solution to confirm that the shRNA was successfully injected in the nucleus. Cytoplasmic removal in Fig. 1 *E–H* and *SI Appendix*, Fig. S2 was performed as previously described (41) and enucleation in Fig. 1 *I–L* and *SI Appendix*, Fig. S3 was adapted from a previous report (15). Hydraulic-controlled glass pipettes mounted on a Piezo-electric drill were used to perforate the zona pellucida of embryos and aspirate either the nucleus (for enucleation) or the cytoplasm without perturbing the nucleus. These procedures were performed in M2 media supplemented with Latrunculin A

5 μM (428021; EMD Millipore). After cytoplasmic removal, at the four-cell stage, sham-manipulated blastomeres displayed on average 32.61 ± 0.24 pL of volume, whereas blastomeres with reduced cytoplasmic size displayed 19.31 ± 0.57 pL (*SI Appendix*, Fig. S2D; average volume reduction of ~40.8%). At the eight-cell stage, sham-manipulated blastomeres displayed on average 16.52 ± 0.74 pL of volume, whereas blastomeres with reduced cytoplasmic size displayed 10.02 ± 0.29 pL (*SI Appendix*, Fig. S2G; average volume reduction of ~40.4%). Embryos were thoroughly washed through at least 10 drops of KSOM prior to being transferred to and cultured in clean KSOM drops prior to imaging.

Immunofluorescence and Live Imaging. Embryos were fixed in 2% paraformaldehyde (P6148; Sigma) diluted in phosphate-buffered saline (PBS) for 20 min followed by 10-min permeabilization using 0.25% Triton X-100 (T9284; Sigma) diluted in PBS and a blocking step with 3% bovine serum albumin (A7906; Sigma) diluted in PBS for either 1 h at 37 °C or overnight at 4 °C (41). Primary antibodies used were PKC ζ anti-mouse 1:100 (sc-17781; Santa Cruz), Anillin anti-rabbit 1:300 (gift from Alisa Piekny, Concordia University, Montréal, Canada); p-Myosin light chain II anti-rabbit 1:100 (3671T; Cell Signaling Technology), and TEAD4 anti-mouse 1:100 (ab58310; Abcam). Hoechst 33342 (1:1,000) (H1399; Invitrogen) was used for DNA labeling and Alexa-labeled secondary antibodies (1:1,000) were purchased from Thermo Fisher. Alexa Fluor 555 Phalloidin (A34055) and Alexa Fluor 647 Phalloidin (A22287) conjugated antibodies (1:200) were purchased from Invitrogen.

Immunofluorescence imaging was performed on a Leica SP8 confocal microscope fitted with a 63× 1.4 numerical aperture oil objective, HyD and PMT detectors and images were acquired using 1.5-μm optical sections and z-stack step size of 1.5 μm. Live imaging was performed on a Leica SP8 confocal microscope fitted with a 20× 0.75 numerical aperture air objective, HyD and PMT detectors and images were acquired with 1-min time intervals using 2.0-μm optical sections and z-stack step size of 2.0 μm. For experiments in Fig. 4, a correlative live and immunofluorescence imaging approach was used as described previously (28), wherein embryos expressing H2B:RFP were subjected to live imaging on either a Leica SP8 confocal microscope fitted with a 20× 0.75 numerical aperture air objective, HyD and PMT detectors or a Zeiss Axio observer equipped with an Axiocam and 20× 0.5 numerical aperture air objective and light-emitting diode light to observe ongoing cell divisions and fixed individually at midcytokinesis (~9 min postanaphase onset) for further immunofluorescence imaging. For all live imaging, embryos were placed on a heated stage top incubator with 5% CO$_2$ supply at 37 °C and imaged in 3-μL drops of pre-equilibrated KSOM.

Image Analysis and Interpretation. Measurements of contractile ring perimeter were performed using IMARIS 9.3 (Bitplane; Oxford Instruments). Using the Oblique Slicer function of IMARIS, the images were slightly rotated and oriented such that the contractile ring was seen from a "face-on" position in a single z-slice and measurements were performed using the Measurement Point function to manually trace the outline of the contractile ring at each timepoint (every 1 min). The contractile ring perimeter was defined as the sum of distances between each Measurement Point outline around the contractile ring. For one-cell embryos, cell divisions always took place such that the contractile ring was parallel from the image plane, and therefore image rotation was deemed not appropriate due to limitations on z-step size resolution that caused deformations on the image and therefore, contractile ring perimeter was calculated based on measurements of ring diameter obtained from a single z-slice and applying the following formula $P = \pi \times d$, where P stands for perimeter, π stands for pi, and d stands for diameter. The duration of cytokinesis was measured as the time between the first frame at which a perimeter decrease was first observed (defined as 5% decrease), until the last frame at which a contractile ring was clearly visible and the perimeter reliably measurable.

Analysis of distance from initial furrow position in Fig. 3 was performed using a single middle z-slice where both sides of the furrow were visible simultaneously. Only blastomeres that were dividing parallel to the coverslip were analyzed. When furrow ingression rate was approximately equal between both sides

of the furrow, the images were rotated in IMARIS, and the same analysis was performed using the portions of the furrow that were not visible in the original plane of analysis to confirm that no bias in furrow ingression was present from another plane (*SI Appendix*, Fig. S6). For measurements of furrow ingression of radial cell divisions in Fig. 3, since no apical and basal sides are present "side 1" was determined as the side of the furrow that was closer to the top of the image in the XY plane and side 2 as the side closer to the bottom of the image.

All experiments involving comparisons of fluorescence intensity between embryos were performed under strictly controlled conditions–simultaneous immunostaining of different samples, same antibody aliquots, concentrations, temperature, time of incubation, as well as confocal imaging performed simultaneously (on the same day) and with identical imaging settings. All fluorescence intensity measurements were performed using Fiji/ImageJ. Apical:basal fluorescence ratios presented in Figs. 2 *F* and *G* and 4 *A–F* and *SI Appendix*, Figs. S2 *H–I*, S4 *B and C, and S8* were calculated using apical and basal maximum gray values from a single z-slice. Background-subtracted total fluorescence intensity (Raw Integrated Density) measurements obtained from a single middle z-slice were used for analysis of apical vs. basal levels of Anillin and p-Myosin in *SI Appendix*, Fig. S7. For confirmation of TEAD4 knockdown efficiency in *SI Appendix*, Fig. S5 *A and B*, nuclear:cytoplasmic ratios were calculated using total fluorescence intensity (Raw Integrated Density) measurements in the nucleus or cytoplasm. For analysis of apical vs. basal levels of PKC ζ and confirmation of TEAD4 knockdown, between 2 and 13 inner and outer blastomeres were quantified per embryo in each group and the data displayed is an average per embryo. For cell volume measurements in *SI Appendix*, Fig. S2 *D and G*, the areas delineated by the cell membrane (GAP43:GFP) were manually traced and measured in each z-slice in blastomeres prior to mitotic entry and the sum of areas was multiplied by the step size (2 μm) to obtain the volume in cubic micrometers and further converted to picoliters, as previously described (41).

For the live-imaging experiments, circumferential cell divisions were classified as those in which the dividing outer cell generated two new outer-residing cells immediately after cytokinesis completion, whereas radial cell divisions were considered as those in which the dividing outer cell generated one new outer-residing and one new inner-residing cell immediately following cytokinesis completion.

Statistical Analysis. All statistical analyses were performed using GraphPad Prism (https://www.graphpad.com/). Shapiro–Wilk normality tests were applied and either parametric or nonparametric statistical tests were applied accordingly. For data encompassing multiple comparisons, either unpaired one-way ANOVA or unpaired Kruskal–Wallis tests corrected for multiple comparisons were applied. For data encompassing two comparisons, either unpaired two-tailed t tests or unpaired two-tailed Mann–Whitney U tests were applied. For analyses of total furrow displacement (Fig. 3 *D and G* and *SI Appendix*, Fig. S6), background-subtracted fluorescence intensity of Anillin and p-Myosin (*SI Appendix*, Fig. S7), either paired two-tailed t test or paired Wilcoxon test were applied. For analyses in Fig. 4F and *SI Appendix*, Fig. S8 *B and D*, one-sample t test was applied for calculations of significant deviation from 1. For *SI Appendix*, Fig. S2J, simple linear regression analysis was applied. Statistical significance was considered when $P < 0.05$.

Data Availability. All study data are included in the article and/or supporting information.

1. F. A. Barr, U. Gruneberg, Cytokinesis: Placing and making the final cut. *Cell* **131**, 847–860 (2007).
2. R. A. Green, E. Paluch, K. Oegema, Cytokinesis in animal cells. *Annu. Rev. Cell Dev. Biol.* **28**, 29–58 (2012).
3. E. Morais-de-Sá, C. Sunkel, Adherens junctions determine the apical position of the midbody during follicular epithelial cell division. *EMBO Rep.* **14**, 696–703 (2013).
4. C. Thieleke-Matos, D. S. Osório, A. X. Carvalho, E. Morais-de-Sá, Emerging mechanisms and roles for asymmetric cytokinesis. *Int. Rev. Cell Mol. Biol.* **332**, 297–345 (2017).

5. N. Founounou, N. Loyer, R. Le Borgne, Septins regulate the contractility of the actomyosin ring to enable adherens junction remodeling during cytokinesis of epithelial cells. *Dev. Cell* **24**, 242–255 (2013).

6. C. Guillot, T. Lecuit, Adhesion disengagement uncouples intrinsic and extrinsic forces to drive cytokinesis in epithelial tissues. *Dev. Cell* **24**, 227–241 (2013).

7. S. N. Jordan *et al.*, Cortical PAR polarity proteins promote robust cytokinesis during asymmetric cell division. *J. Cell Biol.* **212**, 39–49 (2016).

8. C. Cabernard, K. E. Prehoda, C. Q. Doe, A spindle-independent cleavage furrow positioning pathway. *Nature* **467**, 91–94 (2010).

9. K. G. Bourdages, B. Lacroix, J. F. Dorn, C. P. Descovich, A. S. Maddox, Quantitative analysis of cytokinesis in situ during *C. elegans* postembryonic development. *PLoS One* **9**, e110689 (2014).

10. A. Carvalho, A. Desai, K. Oegema, Structural memory in the contractile ring makes the duration of cytokinesis independent of cell size. *Cell* **137**, 926–937 (2009).

11. R. N. Khaliullin *et al.*, A positive-feedback-based mechanism for constriction rate acceleration during cytokinesis in *Caenorhabditis elegans.* eLife **7**, e36073 (2018).

12. A. M. Silva *et al.*, Robust gap repair in the contractile ring ensures timely completion of cytokinesis. *J. Cell Biol.* **215**, 789–799 (2016).

13. M. E. Calvert *et al.*, Myosin concentration underlies cell size-dependent scalability of actomyosin ring constriction. *J. Cell Biol.* **195**, 799–813 (2011).

14. X. Ma *et al.*, Nonmuscle myosin II exerts tension but does not translocate actin in vertebrate cytokinesis. *Proc. Natl. Acad. Sci. U.S.A.* **109**, 4509–4514 (2012).

15. E. Tsichlaki, G. FitzHarris, Nucleus downscaling in mouse embryos is regulated by cooperative developmental and geometric programs. *Sci. Rep.* **6**, 28040 (2016).

16. C. Chazaud, Y. Yamanaka, Lineage specification in the mouse preimplantation embryo. *Development* **143**, 1063–1074 (2016).

17. J. L. Ma^ître, R. Niwayama, H. Turlier, F. Nédélec, T. Hiiragi, Pulsatile cell-autonomous contractility drives compaction in the mouse embryo. *Nat. Cell Biol.* **17**, 849–855 (2015).

18. R. Niwayama *et al.*, A tug-of-war between cell shape and polarity controls division orientation to ensure robust patterning in the mouse blastocyst. *Dev. Cell* **51**, 564–574.e6 (2019).

19. M. H. Johnson, J. C. Chisholm, T. P. Fleming, E. Houliston, A role for cytoplasmic determinants in the development of the mouse early embryo? *J. Embryol. Exp. Morphol.* **97** (suppl.), 97–121 (1986).

20. M. H. Johnson, C. A. Ziomek, Cell interactions influence the fate of mouse blastomeres undergoing the transition from the 16- to the 32-cell stage. *Dev. Biol.* **95**, 211–218 (1983).

21. V. B. Alarcon, Cell polarity regulator PARD6B is essential for trophectoderm formation in the preimplantation mouse embryo. *Biol. Reprod.* **83**, 347–358 (2010).

22. Y. Hirate *et al.*, Polarity-dependent distribution of angiomotin localizes Hippo signaling in preimplantation embryos. *Curr. Biol.* **23**, 1181–1194 (2013).

23. A. I. Mihajlović, V. Thamodaran, A. W. Bruce, The first two cell-fate decisions of preimplantation mouse embryo development are not functionally independent. *Sci. Rep.* **5**, 15034 (2015).

24. S. Anani, S. Bhat, N. Honma-Yamanaka, D. Krawchuk, Y. Yamanaka, Initiation of Hippo signaling is linked to polarity rather than to cell position in the pre-implantation mouse embryo. *Development* **141**, 2813–2824 (2014).

25. J. Rossant, P. P. Tam, Blastocyst lineage formation, early embryonic asymmetries and axis patterning in the mouse. *Development* **136**, 701–713 (2009).

26. T. Frum, A. Ralston, "Pluripotency–What does cell polarity have to do with it?" in *Cell Polarity in Development and Disease*, P. M. Conn, D. W. Houston, Eds. (Elsevier, 2018), chap. 2, pp. 31–60.

27. S. Reinsch, E. Karsenti, Orientation of spindle axis and distribution of plasma membrane proteins during cell division in polarized MDCKII cells. *J. Cell Biol.* **126**, 1509–1526 (1994).

28. C. Vázquez-Diez, G. FitzHarris, Correlative live imaging and immunofluorescence for analysis of chromosome segregation in mouse preimplantation embryos. *Methods Mol. Biol.* **1769**, 319–335 (2018).

29. C. Vázquez-Diez, K. Yamagata, S. Trivedi, J. Haverfield, G. FitzHarris, Micronucleus formation causes perpetual unilateral chromosome inheritance in mouse embryos. *Proc. Natl. Acad. Sci. U.S.A.* **113**, 626–631 (2016).

30. E. Korotkevich *et al.*, The apical domain is required and sufficient for the first lineage segregation in the mouse embryo. *Dev. Cell* **40**, 235–247.e7 (2017).

31. M. Wühr *et al.*, Evidence for an upper limit to mitotic spindle length. *Curr. Biol.* **18**, 1256–1261 (2008).

32. G. Greenan *et al.*, Centrosome size sets mitotic spindle length in *Caenorhabditis elegans* embryos. *Curr. Biol.* **20**, 353–358 (2010).

33. Y. Hara, A. Kimura, Cell-size-dependent spindle elongation in the *Caenorhabditis elegans* early embryo. *Curr. Biol.* **19**, 1549–1554 (2009).

34. K. Yamagata, G. FitzHarris, 4D imaging reveals a shift in chromosome segregation dynamics during mouse pre-implantation development. *Cell Cycle* **12**, 157–165 (2013).

35. J. L. Ma^ître *et al.*, Asymmetric division of contractile domains couples cell positioning and fate specification. *Nature* **536**, 344–348 (2016).

36. A. S. Maddox, L. Lewellyn, A. Desai, K. Oegema, Anillin and the septins promote asymmetric ingression of the cytokinetic furrow. *Dev. Cell* **12**, 827–835 (2007).

37. S. Herszterg, A. Leibfried, F. Bosveld, C. Martin, Y. Bellaiche, Interplay between the dividing cell and its neighbors regulates adherens junction formation during cytokinesis in epithelial tissue. *Dev. Cell* **24**, 256–270 (2013).

38. X. F. Liu, H. Ishida, R. Raziuddin, T. Miki, Nucleotide exchange factor ECT2 interacts with the polarity protein complex Par6/Par3/protein kinase Czeta (PKCzeta) and regulates PKCzeta activity. *Mol. Cell. Biol.* **24**, 6665–6675 (2004).

39. A. I. Mihajlović, A. W. Bruce, Rho-associated protein kinase regulates subcellular localisation of Angiomotin and Hippo-signalling during preimplantation mouse embryo development. *Reprod. Biomed. Online* **33**, 381–390 (2016).

40. G. Fitzharris, A shift from kinesin 5-dependent metaphase spindle function during preimplantation development in mouse. *Development* **136**, 2111–2119 (2009).

41. C. Vázquez-Diez, L. M. G. Paim, G. FitzHarris, Cell-size-independent spindle checkpoint failure underlies chromosome segregation error in mouse embryos. *Curr. Biol.* **29**, 865–873.e3 (2019).